ORIGINAL PAPER



Early-Time Shut-In for Plane-Strain Hydraulic Fractures

Received: 3 January 2023 / Accepted: 20 March 2023 © The Author(s) 2023

Abstract

One investigates the post-shut-in growth of a plane-strain hydraulic fracture in an impermeable medium while accounting for the possible presence of a fluid lag. After the stop of fluid injection, the fracture may present three distinct propagation patterns: an immediate arrest, a temporary arrest with delayed propagation, and a continuous fracture growth. These three patterns are all followed by a final fracture arrest yet the fracture behaviour prior to that results from the interplay between the dimensionless toughness \mathcal{K}_m , the shut-in time t_s/t_{om} , and the propagation time t/t_s . \mathcal{K}_m characterizes the energy dissipation ratio between fracture surface creation and viscous fluid flow under constant rate injection. t_s and t_{om} represent respectively the timescale of shut-in and the coalescence of the fluid and fracture fronts. The immediate arrest occurs when the fracture toughness dominates the fracture growth at the stop of injection ($\mathcal{K}_m \gtrsim 4.3$). It may also occur upon an early shut-in at low dimensionless toughness associated with an overshoot of fracture extension and a significant fluid lag. For intermediate values of \mathcal{K}_m and t_s/t_{om} , the fracture may experience a temporary arrest followed by a restart of fracture propagation. The period of the temporary arrest becomes shorter with higher dimensionless toughness and later shut-in until it drops to zero. The fracture behaviour after shut-in then transitions from temporary arrest to continuous propagation. These propagation patterns result in different evolution of fracture dimensions which possibly explains the various emplacement scaling relations reported in magmatic dikes.

Highlights

Published online: 03 April 2023

- Transitional pulse solutions for plane-strain hydraulic fractures with zero lag
- Immediate fracture front arrest upon shut-in associated with an overshoot of fracture extension
- Temporary fracture arrest and step-wise fracture growth after shut-in in the presence of a fluid lag

Keywords Shut-in · Fluid lag · Cavitation · Fracture arrest · Step-wise fracture propagation

List of Symbo	ls	$F(s_i), \mathbf{F}$	Non-singular unknowns correspond-
C_L, C'	Fluid loss constant and its cor-	,	ing to the s-grid
	responding effective leak-off	$\mathcal{G}_e, \mathcal{G}_m, \mathcal{G}_k, \mathcal{G}_o, \mathcal{G}_l, \mathcal{G}_v$	Dimensionless groups for elasticity,
	coefficient		lubricated fluid flow, fracture tough-
\mathbb{D}	z -grid differentiation operator		ness, minimum confining stress, fluid
E, E'	Elastic modulus and plane-strain		extent and fluid mass conservation
	elastic modulus	H	Hilbert transform operator
		$K_{ m I}$	Mode I stress intensity factor
		$K_{\rm Ic}, K'$	Fracture toughness and effective
□ Dong Liu			fracture toughness
dong.liu@ucl	l.ac.uk	$\mathcal{K}_m, \mathcal{K}_m^{[V]}$	Dimensionless toughness for a con-
Department of Earth Sciences, University College London, London, UK		<i></i>	tinuous injection without shut-in and a pulse injection with shut-in



0	For all the left leavests
ℓ	Fracture half-length
ℓ_f	Half length of the fluid extent
ℓ_s	Fracture half-length at shut-in
ℓ_a	Fracture half-length at arrest
L, L_f, P, W	Characteristic scales for the fracture
	length, fluid extent, net pressure, and
	fracture opening
n	Number of points for the s-grid
p_f, p	Fluid pressure and net pressure
p_a	Net pressure at fracture arrest
q	Local fluid flux inside the fracture
Q	Extrapolation operator at $z_i = 1$
Q_o	Fluid injection rate
$S_j, \mathbf{S}; \mathcal{Z}_i, \mathbf{Z}$	Primary and complimentary set of
	spatial nodes in Gauss-Chebyshev
	quadrature
\mathbb{S}_A	s -grid integration operator on $[-1, 1]$
\mathbb{S}_A	s -grid integration operator on $[-1, z_i]$
t_c	Critical shut-in time at which the
	fracture length equals the theoretical
	arrest length $\ell_s/\ell_a = 1$
$t_{mk}^{[V]}$	Timescale characterizing the transi-
*****	tion from the shut-in to the final
	fracture arrest
$t_{m ilde{m}}$	Timescale characterizing the transi-
	tion from storage growth regimes to
	leak-off regimes
t_{om}	Timescale characterizing the coales-
	cence of the fracture and fluid fronts
t_r	Restart time of fracture propagation
	after shut-in
t_{s}	Shut-in time
T_k	Gauss-Chebyshev polynomials of
	the first kind
V	Fracture volume
V_f	Injected fluid volume
${V}_s$	Fracture volume at shut-in
W	Fracture opening
w_a	Fracture opening at fracture arrest
x, x'	Fracture coordinate
γ	Dimensionless fracture half-length
γ_f	Dimensionless half-length of the
,	fluid extent
ζ	Dimensionless shut-in time t_s/t_{om}
θ	State variable related to fluid
	cavitation
μ, μ'	Fluid viscosity and effective
	viscosity
ν	Poisson's ratio
ξ, ξ'	Dimensionless fracture coordinate
=	

ثع	Dimensionless fracture coordi-
	nate with respect to the fluid front
	position
ξ_f	Fluid fraction
$\H{\Pi}$	Dimensionless net pressure
σ_o	Minimum confining stress perpen-
	dicular to the fracture plane
Ψ	Dimensionless local fluid flux inside
	the fracture
ω	Weight function of Gauss-Cheby-
	shev quadratures
Ω	Dimensionless fracture opening

1 Introduction

Hydraulic fractures are tensile fractures generated by viscous fluid injection. They exist widely in nature, such as during the formation of magma dikes and sills and the drainage of glacier lakes, and industrial applications, such as oil and gas extraction, CO₂ storage, and enhanced geothermal systems. During the propagation of hydraulic fractures, a fluid-less cavitation exists near the fracture tip and removes the pressure singularity inside the viscous fluid flow. This cavitation, denoted as the fluid lag, dominates the hydraulic fracture growth at early time and gradually vanishes as the fluid front catches up with the fracture front. The fluid lag is often neglected in the context of deep reservoirs due to large confinement, yet can be essential (i) in some laboratory hydraulic fracturing experiments (Bunger et al. 2013; Liu et al. 2020; Liu 2021; Liu and Lecampion 2023) and near-surface hydraulic fracture propagation (Bunger and Detournay 2007; Zhang et al. 2002, 2005; Lecampion and Detournay 2007; Gordeliy and Detournay 2011; Gordeliy et al. 2019; Chen et al. 2018; Wang and Detournay 2018, 2021. (ii) It also plays an important role in the interplay with a rough process zone which deviates the viscous fluid flow from Poiseuille's law and leads to additional energy dissipation (Liu and Lecampion 2019a, b, 2021). (iii) Moreover, it also presents during the formation of magma-driven geological structures, with magma being an extremely viscous intrusion fluid leading to a fluid-less cavitation (Rubin 1993, 1995; Rivalta and Dahm 2006; Bunger and Cruden 2011).

These circumstances, especially the laboratory hydraulic fracturing injection and the formation of magma dikes and sills, are often associated with a fluid shut-in or a pulse injection. However, few studies on the post-shut-in growth of hydraulic fractures have accounted for the possible presence of a fluid lag. Garagash (2006a) and Liu and Lu (2023) investigate the arrest dynamics of a plane-strain hydraulic fracture after shut-in in the limit of large toughness and zerotoughness respectively. Furthermore, recent work (Möri and



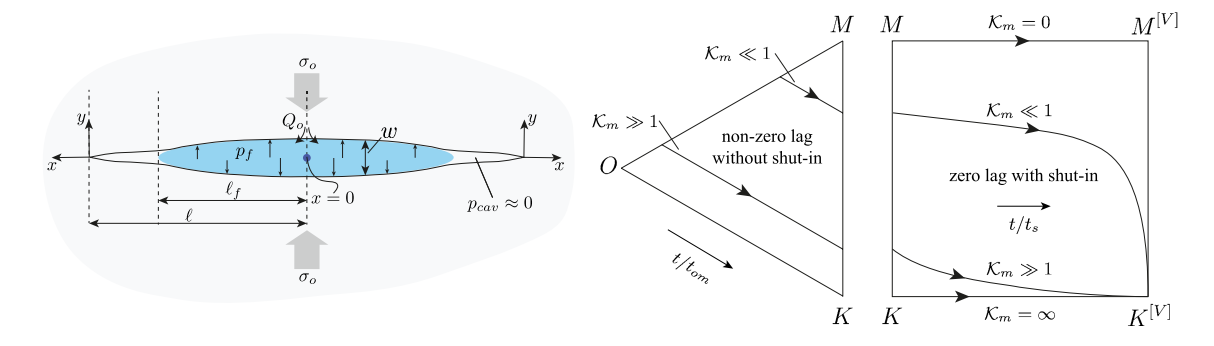


Fig. 1 Illustration of the growth of a plane-strain hydraulic fracture with the possible presence of a fluid lag and propagation schemes for a continuous injection and a fluid shut-in. The superscript [V] is associated with a fluid shut-in/pulse injection

Lecampion 2021; Peirce and Detournay 2022a, b; Peirce 2022) studies the arrest and recession dynamics of a plane-strain/semi-infinite/radial hydraulic fracture after shut-in allowing for fluid leak-off. All these studies assume zero fluid lag, and the post-shut-in fracture behaviour with a fluid lag remains unknown.

Previous studies (Möri and Lecampion 2021; Liu and Lu 2023, for example) dealing with the stop of fluid injection often assume a constant injection rate before the shut-in. The same assumption is made in this study. As a result, the fracture growth before the shut-in follows the same way as the constant-rate-injection solutions. As discussed in Spence and Sharp (1985); Garagash (2006b); Lecampion and Detournay (2007), the growth of a plane-strain hydraulic fracture in an impermeable medium evolves from an early-time solution where the fluid lag is maximum to a late-time solution where the fluid and fracture fronts coalesce (zero lag case) over a timescale

$$t_{om} = \frac{E'^2 \mu'}{\sigma_o^3} \tag{1}$$

where $E' = E/(1 - v^2)$ is the plane-strain modulus, v the Poisson's ratio of the material, $\mu' = 12\mu$ the effective fluid viscosity, and σ_o the minimum confining stress. As the fluid and fracture fronts coalesce at $t/t_{om} \rightarrow 1$, the fracture growth transitions to zero-lag solutions. These zero-lag solutions present self-similar characteristics and solely depend on a dimensionless toughness \mathcal{K}_m which describes the energy dissipation ratio between the creation of fracture surfaces and the viscous fluid flow (Garagash and Detournay 2005; Garagash 2006a).

$$\mathcal{K}_m = \frac{K'}{E'} \left(\frac{E'}{\mu' Q_o} \right)^{1/4} \tag{2}$$

where $K' = \sqrt{32/\pi} K_{\rm Ic}$ indicates the effective fracture toughness and Q_o the constant fluid injection rate. As a result of the viscous fluid flow, the fluid lag can be significant for

smaller values of the dimensionless toughness and dimensionless time t/t_{om} . It can be however negligible at all times for high dimensionless toughness when toughness dominates the fracture growth. One illustrates such propagation of a plane-strain hydraulic fracture in Fig. 1 via a triangular phase diagram. The O-, M-, and K-vertex correspond respectively to the limiting case of a significant lag/negligible toughness, the viscosity-dominated propagation with zero fluid lag, and the toughness-dominated propagation where viscous effects are always negligible. These vertex analytical solutions are given in Garagash (2006b, 2006a) and Garagash and Detournay (2005).

In this paper, one tries to extend the analytical framework of the plane-strain hydraulic fracture growth with a fluid lag by focusing on the post-shut-in stage assuming zero leak-off. One shows that three possible post-shut-in propagation patterns may occur after the shut-in depending on the dimensionless toughness and shut-in time: an immediate arrest, a temporary arrest with a restart of propagation, and a continuous fracture extension. One investigates the evolution of fluid pressure, fracture dimensions, and emplacement scaling relations throughout the shut-in process and discusses the possible boundaries between different propagation patterns in the parametric space of the dimensionless toughness and shut-in time.

2 Problem Formulation

This study assumes that the fracture propagates in an infinite linear elastic medium characterized by the elastic modulus E, Poisson's ratio v, and fracture toughness $K_{\rm Ic}$. The fracture grows subjected to uniform far-field stress σ_o . It is driven by a constant-rate Q_o fluid injection until a shut-in occurs at $t = t_s$. The fluid is incompressible and Newtonian with a dynamic viscosity of μ . The leak-off of injection fluid into the surrounding medium/reservoir is neglected, and the



pressure of the fluid cavitation is approximated as zero—the same as illustrated in Fig. 1.

For clarity, one keeps the same definitions of effective parameters as already introduced in the previous section and in Detournay (2016, and references therein) by setting

$$E' = \frac{E}{1 - v^2}, K' = \sqrt{\frac{32}{\pi}} K_{\rm Ic}, \mu' = 12\mu.$$
 (3)

They correspond respectively to the plain-strain elastic modulus, the effective toughness, and the effective viscosity.

2.1 Elastic Deformation

The quasi-static balance of momentum relates the fracture opening w(x, t) and the net pressure $p_f(x, t) - \sigma_o$ (the difference between the fluid pressure and the far field confining stress) via a boundary integral equation (see for example Hills et al. 1996). In view of the problem symmetry, it can be written on one wing of the fracture:

$$\frac{E'}{4\pi} \int_0^{\ell} \left(\frac{1}{x - x'} - \frac{1}{x' + x} \right) \frac{\partial w(x', t)}{\partial x'} dx'$$

$$= p_f(x, t) - \sigma_o, x, x' \in [0, \ell]$$
(4)

where ℓ is the half-length of the plane-strain fracture.

2.2 Propagation Criterion

The propagation mechanism is modulated by a constant fracture toughness following the linear elastic fracture mechanics by assuming a negligible non-linear process zone. The stress intensity factor $K_{\rm I}$ must equal the fracture toughness $K_{\rm Ic}$ at any given time during the propagation and can only stay below the toughness when the fracture is at arrest. As a consequence, the following condition must be satisfied at all times.

$$(K_{\rm I} - K_{\rm Ic})\dot{\ell} = 0, \ \dot{\ell} \ge 0$$
 (5)

 $K_{\rm I} = K_{\rm Ic}$ can be alternatively expressed in the form of the classical square-root asymptote near the fracture tip (Rice 1968).

$$w \sim \frac{K'}{E'} (\ell - x)^{1/2}, \ \ell - x \ll \ell \tag{6}$$

2.3 Continuity

Assuming zero compressibility, the fluid mass conservation in the elastic deformable fracture reduces to



where $\ell_f(t)$ denotes the current fluid front position, and q(x, t) the local fluid flux inside the fracture. The fluid is injected at the fracture center under a constant injection rate Q_o (in m²/s under plane-strain conditions) until a shut-in occurs at $t = t_s$. The flux entering one wing of the fracture thus writes:

$$q(x = 0^{+}) = \begin{cases} Q_o/2, & t < t_s \\ 0, & t \ge t_s \end{cases}$$
 (8)

which can be translated into the form of the global fluid volume balance by integrating the continuity Eq. (7) for the fluid:

$$2\int_0^{\ell_f(t)} w(x,t) \mathrm{d}x = V_f \tag{9}$$

with

$$V_f = \begin{cases} Q_o t, & t < t_s \\ Q_o t_s, & t \ge t_s. \end{cases}$$
 (10)

2.4 Poiseuille's Law

Under the assumption of a Newtonian fluid and a laminar flow inside the fracture, the fluid flux can be approximated by Poiseuille's law:

$$q = -\frac{w^3}{\mu'} \frac{\partial p_f}{\partial x}, \quad 0 < x < \ell_f \tag{11}$$

2.5 Fluid Lag

The fluid front lags behind the fracture front with its velocity $\dot{\ell_f}$ equal to the mean fluid velocity q/w at $x = \ell_f$ (Stefan condition):

$$\dot{\ell_f} = -\frac{w^2}{\mu'} \frac{\partial p_f}{\partial x} \text{ at } x = \ell_f$$
 (12)

The fluid is vaporized inside the fluid lag with a cavitation pressure p_{cav} much smaller than the liquid pressure p_f in the fluid-filled part and the in-situ confining stress σ_o .

$$p_f(x,t) = p_{cav} \approx 0, \quad x \in [\ell_f(t), \ell(t)]$$
(13)

2.6 Boundary Conditions

The fracture opening and fluid flux are zero at the fracture tip.



$$w(x = \ell, t) = 0, \ q(x = \ell, t) = 0$$
 (14)

2.7 Initial Conditions

One models the fluid lag nucleation starting from a negligibly small fracture. The initial conditions correspond to the linear elastic solutions of a uniformly pressurized static flaw with a fluid pressure slightly larger than the in-situ stress σ_o $((p_f - \sigma_o)/\sigma_o \ll 1)$.

3 Structure of the Solution

One discusses in this section the post-shut-in growth of a plane-strain hydraulic fracture in light of dimensional analysis. One notably highlights the difference brought by the fluid cavitation and the shut-in of fluid injection compared to the zero-lag continuous-injection solutions (Detournay 2004; Garagash and Detournay 2005; Garagash 2006a, b). Following Liu and Lecampion (2021), one scales the flux q with the injection rate Q_o , and scales the fracture width w, net pressure $p_f - \sigma_o$, fracture length ℓ , and the extent of the liquid-filled part of the fracture ℓ_f by introducing corresponding width W, pressure P, fracture length L and fluid extent L_f characteristic scales:

$$w(x,t) = W(t) \Omega(\xi, \mathcal{P}), p_f(x,t) - \sigma_o = P(t) \Pi(\xi, \mathcal{P})$$

$$q(x,t) = (V_f/t) \Psi(\xi, \mathcal{P}), \ell(t) = L(t) \gamma(\mathcal{P}), \ell_f(t) = L_f(t) \gamma_f(\mathcal{P})$$
(15)

where $\xi = x/\ell$ is a dimensionless coordinate. The dimensionless variables depend on one or more dimensionless numbers \mathcal{P} (which may depend on time). Introducing such a scaling relation in the governing equations of the problem allows one to isolate different dimensionless groups associated with the different physical mechanisms at play (elasticity, injected volume, viscosity, fracture toughness) and define relevant scalings.

Before going further, one briefly lists the dimensionless form of the governing equations where appear different dimensionless groups.

• Elasticity (4)

$$\Pi = \mathcal{G}_e \frac{1}{4\pi} \frac{1}{\gamma} \int_0^1 \frac{\partial \Omega}{\partial \xi} \left(\frac{1}{\xi - \xi'} - \frac{1}{\xi + \xi'} \right) d\xi',$$

$$0 < \xi, \xi' < 1$$
(16)

Propagation condition (6)

$$\Omega \sim \mathcal{G}_k \gamma^{1/2} (1 - \xi)^{1/2}, \quad 1 - \xi \ll 1$$
 (17)

• Fluid continuity (7) and Poiseuille's law (11)

$$t\frac{\partial\Omega}{\partial t} + t\frac{\dot{W}}{W}\Omega + \mathcal{G}_{v}\frac{1}{\gamma_{f}}\frac{\partial\Psi}{\partial\hat{\xi}} = 0$$
 (18)

$$\Psi = -\frac{1}{\mathcal{G}_m} \frac{\Omega^3}{\gamma_f} \frac{\partial \Pi}{\partial \hat{\varepsilon}} \tag{19}$$

with $\hat{\xi} = x/\ell_f = \xi \times (\gamma/\gamma_f)/\mathcal{G}_l$ the spatial coordinate with respect to the fluid front position.

• Fluid lag (13)

$$\Pi(\xi \ge \xi_f = \ell_f/\ell) = -\mathcal{G}_o \tag{20}$$

The solution of the problem thus depends on the following dimensionless groups.

$$\begin{aligned} \mathcal{G}_{e} &= \frac{WE'}{PL}, \quad \mathcal{G}_{k} = \frac{K'L^{1/2}}{E'W}, \quad \mathcal{G}_{v} = \frac{V_{f}}{WL_{f}}, \quad \mathcal{G}_{m} = \frac{\mu'V_{f}L_{f}}{PW^{3}t}, \\ \mathcal{G}_{o} &= \frac{\sigma_{o}}{P}, \quad \mathcal{G}_{l} = \frac{L_{f}}{L} \end{aligned} \tag{21}$$

One sets $\mathcal{G}_e=1$ and $\mathcal{G}_v=1$ by recognizing that elasticity is always important and that the fracture volume equals the injected volume at all times. Assuming a negligible fluid lag $(\mathcal{G}_l=L_f/L=1)$, one obtains the viscosity and toughness scalings by setting respectively \mathcal{G}_m ($M^{[V]}$ /viscous scaling) and \mathcal{G}_k ($K^{[V]}$ /toughness scaling) to unity (The superscript [V] denotes the scaling commensurate with a fluid shut-in at time t_s and an injection volume of V_f). The fluid lag dominated scaling ($O^{[V]}$ -vertex) is obtained by setting $\mathcal{G}_m=1$

Table 1 Characteristic scales and dimensionless numbers governing the evolution of a plane-strain hydraulic fracture after shut-in for different limiting regimes: $O^{[V]}$ —the lag/viscosity dominated regime, $M^{[V]}$ —the fully filled/viscosity dominated regime, and $K^{[V]}$ —the fully filled/toughness dominated regime

	$O^{[V]}$	$M^{[V]}$	$K^{[V]}$	
L	$\frac{E'\mu'^{1/4}V_f^{1/2}}{\sigma_o^{5/4}t^{1/4}}$	$\frac{E'^{1/6}V_f^{1/2}t^{1/6}}{\mu'^{1/6}}$	$\frac{E'^{2/3}V_f^{2/3}}{K'^{2/3}}$	
P	σ_o	$\frac{E'^{2/3}\mu'^{1/3}}{t^{1/3}}$	$\frac{K'^{4/3}}{E'^{1/3}V_f^{1/3}}$	
W	$\frac{\mu'^{1/4}V_f^{1/2}}{\sigma_o^{1/4}t^{1/4}}$	$\frac{\mu'^{1/6}V_f^{1/2}}{E'^{1/6}t^{1/6}}$	$\frac{K'^{2/3}V_f^{1/3}}{E'^{2/3}}$	
L_{f}/L	$(t/t_{om})^{1/2}$	1	1	
\mathcal{G}_m	1	1	$\mathcal{K}_m^{[V]-4}$	
\mathcal{G}_k	$\mathcal{K}_m^{[V]} (t/t_{om})^{-1/8}$	$\mathcal{K}_m^{[V]}$	1	
\mathcal{G}_o	1	$(t/t_{om})^{1/3}$	$(t/t_{om})^{1/3}\mathcal{K}_m^{[V]-4/3}$	

The timescale t_{om} is defined in Eq. (1) and the dimensionless toughness under a pulse injection $\mathcal{K}_{m}^{[V]}$ is defined in Eq. (23)



and $\mathcal{G}_o=1$ recognizing that viscous effects are necessary for cavitation to occur and that the lag covers a significant part of the fracture such that the pressure scale is given by the in-situ stress. One shows the scalings for these limiting propagation regimes in Table 1. When replacing $V_f=Q_ot$, one recovers the same scaling relations for a continuous injection (Detournay 2004; Garagash and Detournay 2005; Garagash 2006a, b).

Two timescales emerge from the scaling analysis: $t_{om}(1)$ as the time for the dimensionless in-situ stress \mathcal{G}_o to reach unity, which characterizes the disappearance of the fluid lag, and $t_{mk}^{[V]}$ characterizing the transition from the shut-in to the final fracture arrest.

$$t_{mk}^{[V]} = \frac{E'^3 \mu' V_f}{K'^4} \tag{22}$$

One further obtains the dimensionless toughness corresponding to a pulse injection:

$$\mathcal{K}_{m}^{[V]} = \left(\frac{t}{t_{mk}^{[V]}}\right)^{1/4} = \frac{K'}{E'} \left(\frac{E't}{\mu' V_{f}}\right)^{1/4} = \mathcal{K}_{m} \left(\frac{t}{t_{s}}\right)^{1/4}$$
(23)

which embeds \mathcal{K}_m (2) the dimensionless toughness describing the energy dissipation between fracture surface creation and viscous fluid flow at the time of shut-in, and the time t/t_s of fracture propagation following the stop of injection. For the post-shut-in stage $(t/t_s > 1)$, $\mathcal{K}_m^{[V]}$ increases monotonically from \mathcal{K}_m representing a transition to a fracture behaviour more dominated by the fracture toughness. This is consistent with the uniform pressure inside the fracture at final arrest, which implies negligible energy dissipation in the viscous fluid flow.

The complete evolution of the solution between different regimes is then grasped by the dimensionless toughness \mathcal{K}_m upon shut-in, the dimensionless time t/t_{om} , and the dimensionless shut-in moment.

$$\zeta = \frac{t_s}{t_{om}} = \frac{t_{mk}^{[V]}}{t_{om}} \mathcal{K}_m^4 \tag{24}$$

 ζ characterizes how far the fluid front lags behind the fracture front at the time of shut-in: $\zeta \ll 1$ represents a significant fluid lag and $\zeta \gg 1$ indicates the limit of zero fluid lag. Depending on the combinations of \mathcal{K}_m and ζ , different fracture behaviour can be expected:

• When $\zeta \gg 1$, the fluid and fracture fronts coalesce with zero fluid lag. For $\mathcal{K}_m \ll 1$, the fracture growth follows the zero-toughness pulse-injection solutions ($M^{[V]}$ -solution) obtained by Liu and Lu (2023) where the propagation continues without arrest. For $\mathcal{K}_m \gg 1$, the fracture growth is dominated by fracture toughness at

- the time of shut-in and the pressure is uniform everywhere inside the fracture. This leads to an immediate arrest of the fracture growth upon shut-in ($K^{[V]}$ -solution). For intermediate values of \mathcal{K}_m , the fracture continues to propagate until the final arrest.
- When $\zeta \ll 1$, the shut-in occurs at early time and a non-negligible fluid lag exists regardless of the value of the dimensionless toughness \mathcal{K}_m . The fracture behaviour will result from the interplay between the dimensionless toughness \mathcal{K}_m , the shut-in moment $\zeta = t_s/t_{om}$, and the dimensionless time t/t_{om} .

The zero-lag transitional solutions ($\zeta \gg 1$) with intermediate values of \mathcal{K}_m and the post-shut-in solutions in the presence of a fluid lag ($\zeta \ll 1$) will be now investigated numerically.

4 Numerical Scheme

One adopts two different numerical schemes depending on whether there is a significant fluid lag during the fracture growth.

In absence of a fluid lag, one uses a spectral method based on the Gauss-Chebyshev quadrature and Barycentric interpolation techniques (Viesca and Garagash 2018; Liu et al. 2019). This method turns the coupled fracture problem into a series of ordinary differential equations, with its initial conditions set as the self-similar solutions of a plane-strain hydraulic fracture for a constant dimensionless toughness (Garagash and Detournay 2005; Garagash 2006a). The mathematical formulation for the zero-lag fracture problem remains the same as presented in Sect. 2 except for $\ell_f = \ell$. One refers to Appendix 1 for their detailed discretization.

When accounting for a fluid lag, one uses an Elrod-Adams type scheme based on a fixed regular grid with a constant mesh size following Mollaali and Shen (2018) and Liu and Lecampion (2019a, 2019b, 2021). This scheme introduces a fluid state variable $\theta \in [0, 1]$ (1 for the liquid phase, 0 for the vapour phase) in a similar way to thin-film lubrication cavitation models (see Szeri 2010, for example). It automatically captures the spontaneous nucleation of the fluid lag by imposing additional inequalities conditions ($p_f \ge 0$, $0 \le \theta \le 1$, $p_f(1 - \theta) = 0$) in each element. The elasticity and fluid mass conservation is then discretized respectively using a displacement discontinuity method with piece-wise constant elements and finite difference. One uses an implicit time-integration scheme to solve iteratively for the fluid pressure and the associated opening. The solution is obtained using three nested iterative loops for a fixed increment of fracture length before the shut-in: one starts from a trial time step and solves the fluid pressure for all elements



inside the fracture using a quasi-Newton method. Such a procedure is repeated until each element in the fracture reaches a consistent state: either fluid or vapor. The time step is finally adjusted in an outer loop using a bi-section and secant method to fulfill the propagation criterion. One refers the details of the numerical solver to Liu and Lecampion (2021) and discusses the model validation in Appendix 2.

One applies the fluid shut-in via the fracture length by controlling the activated number of elements: when the fracture length goes beyond the shut-in length $\ell \geq \ell_s = \ell(t=t_s)$, the injection is stopped. After shut-in, one solves the non-linear system with an assumed time step and checks afterwards whether the propagation condition is fulfilled at the fracture tip: the fracture front advances only when $K_I \geq K_{Ic}$. This allows for both a temporary and a permanent stop of the fracture extent yet an exact solution for the final arrest time (or the restart propagation time) necessitates a small time step and a fine mesh.

5 Results and Discussion

5.1 Zero-Lag Vertex Solutions

When the fracture toughness dominates the propagation at the time of shut-in ($\mathcal{K}_m\gg 1$), the fluid pressure is uniform inside the fracture with the stress intensity factor equal to the fracture toughness. Any further fracture extension will lead to a drop in the stress intensity factor and an immediate arrest. The fracture behaviour (the pulse toughness-dominated solution or the $K^{[V]}$ -vertex solution) thus corresponds to the solution of a linear elastic fracture under uniform far-field load. The fracture half-length ℓ_a , the fracture opening w_a and the net pressure at arrest write as follows.

$$\ell_a = \frac{2}{\pi^{2/3}} \left(\frac{E'V_f}{K'} \right)^{2/3} \tag{25}$$

$$w_a = \frac{1}{\pi^{1/3}} \left(\frac{{K'}^2 V_f}{E'^2} \right)^{1/3} \sqrt{1 - \xi^2}$$
 (26)

$$p_a = \frac{\pi^{1/3}}{8} \left(\frac{K'^4}{E'V_f} \right)^{1/3} \tag{27}$$

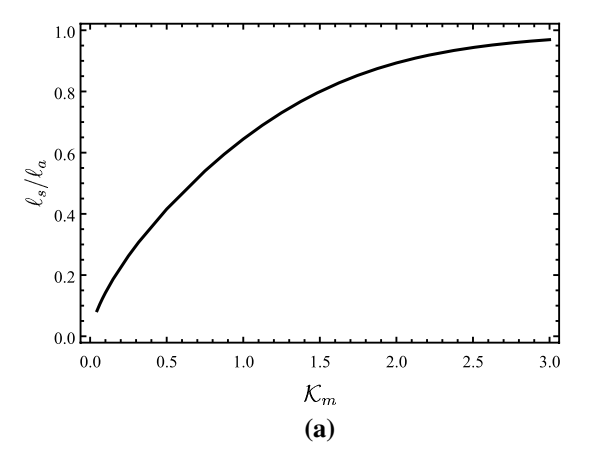
In absence of a fluid lag, the fracture propagates without arrest when the fracture toughness is zero $K_{\rm Ic}=0$. The solution, denoted as the pulse viscosity dominated solution or the $M^{\rm [V]}$ -vertex solution, is self-similar and has been obtained numerically using the Gauss–Chebyshev quadrature and Barycentric interpolation techniques in Liu and Lu (2023). One recalls here the expression for the fracture half-length.

$$\ell \approx 0.8026 \frac{E'^{1/6} V_f^{1/2} t^{1/6}}{\mu'^{1/6}} \tag{28}$$

The $M^{[V]}$ -vertex solution implies that the fracture half-length evolves with time in a way that $\ell \sim t^{1/6}$. Note that such a time evolution of the fracture length may also appear during the transition to the final fracture arrest for $K_{\rm Ic}>0$ as shown in Fig. 2.

5.2 Zero-Lag Transitional Solutions

In absence of a fluid lag, the fracture with a finite non-zero toughness continues to grow after shut-in, with the elastic energy stored prior to the shut-in partially balanced by the creation of new fracture surfaces. Such post-shut-in fracture growth stops when the fracture length reaches the $K^{[V]}$ -solution



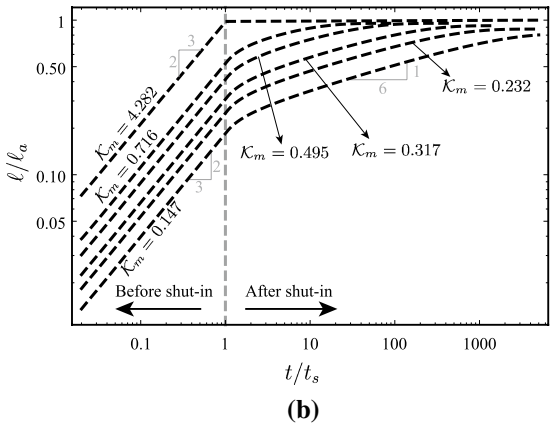


Fig. 2 Evolution of the fracture length ratio between the shut-in and final arrest in function of a the dimensionless toughness and b the dimensionless time in absence of a fluid lag

at $\ell = \ell_a$. Approximating the fracture half-length ℓ_s at shut-in with the self-similar solutions (Garagash and Detournay 2005; Garagash 2006a) (by assuming that the plane-strain fracture is driven under a constant injection rate before shut-in), one defines $1 - \ell_s / \ell_a$ as the potential fracture extension after the stop of fluid injection.

$$\frac{\ell_s}{\ell_a} = \frac{\gamma_m L_m}{\ell_a} = \frac{\pi^{2/3}}{2} \gamma_m \mathcal{K}_m^{2/3} \tag{29}$$

where γ_m is the self-similar solution for constant injection rate in the viscosity dominated scaling (Garagash and Detournay 2005; Garagash 2006a) and L_m the length scale in the viscosity scaling as shown in Table 1. This ratio of the fracture length ℓ_s/ℓ_a is solely a function of the dimensionless toughness \mathcal{K}_m . As illustrated in Fig. 2a, when $\mathcal{K}_m \gtrapprox 2.596$, the fracture half-length ℓ_s is equal to or larger than 95% of the final arrest fracture half-length ℓ_a , and the fracture front could barely advance after the stop of fluid injection.

One further investigates numerically the post-shut-in growth of a plane-strain hydraulic fracture and its subsequent arrest employing a spectral solver. One displays in Fig. 2b the evolution of the fracture half-length as a function of t/t_s for different values of \mathcal{K}_m . For small values of \mathcal{K}_m , the hydraulic fracture is in the viscosity dominated regime when the shut-in occurs. One observes a transition from the small toughness solution (with $\ell \sim t^{2/3}$) (Garagash 2006a) to the pulse viscosity dominated solution (28) (with $\ell \sim t^{1/6}$) (Liu and Lu 2023). Such a transition is much shortened for larger values of \mathcal{K}_m , where more energy dissipation is owed to the creation of fracture surfaces. For $\mathcal{K}_m \gtrsim 4.3$ (Garagash 2006a), the fracture growth is dominated by fracture toughness at the time of shut-in, leading to an immediate arrest. A diagram describing such post-shut-in propagation

of a plane-strain hydraulic fracture with zero fluid lag is illustrated in Fig. 1 together with that of a continuous fluid injection.

5.3 Non-zero Fluid Lag Solutions with Shut-In

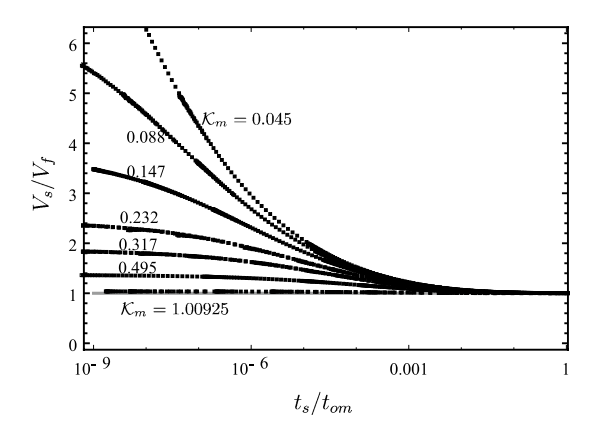
In this section, one focuses on the post-shut-in growth accounting for the presence of a non-negligible fluid lag. The fluid lag can be significant for small and intermediate values of dimensionless toughness especially when the shut-in occurs at the early time of hydraulic fracture growth. To better describe the fracture behaviour after the shut-in, one defines the volume efficiency coefficient as the ratio between the total volume of the created fracture V and the injected fluid volume V_f .

$$\frac{V}{V_f} = \frac{2}{V_f} \int_0^\ell w(x) \mathrm{d}x \tag{30}$$

One also defines the length efficiency coefficient ℓ/ℓ_a as the ratio between the fracture half-length ℓ and the fracture half-length at arrest ℓ_a under the pulse injection.

The post-shut-in fracture behaviour is a function of both the dimensionless toughness and dimensionless shut-in time. One shows in Fig. 3 the volume and length efficiency parameters upon shut-in as a function of these two dimensionless parameters. Note that these results only describe the fracture growth at the shut-in time, neither before nor after.

The volume efficiency is always greater than one owing to a non-zero volume of the fluid cavitation. A more significant effect of the viscous fluid flow or a larger dimensionless toughness \mathcal{K}_m tends to lead to a more efficient injection with the fracture volume larger than the volume of injected fluid. The volume efficiency decreases towards



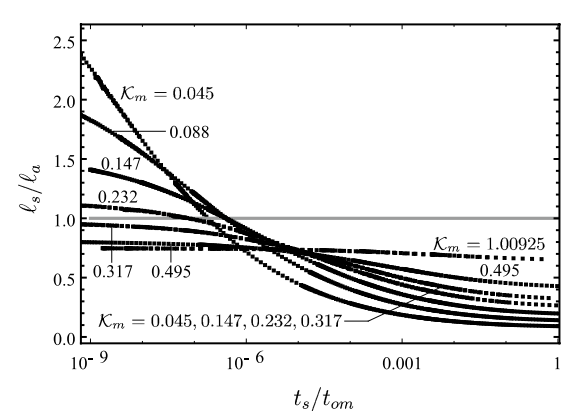


Fig. 3 Evolution of the volume V_s/V_f and length ℓ_s/ℓ_a efficiency coefficients at different shut-in time t_s/t_{om} accounting for the presence of a fluid lag



one as the shut-in occurs later, and the fluid front tends to catch up with the fracture front until the fracture is fully filled with fluid.

The fracture length efficiency also decreases as the shut-in occurs later (Fig. 3). When the effect of viscous fluid flow is more dominant during the fracture growth (smaller dimensionless toughness \mathcal{K}_m values), the decrease in length efficiency becomes more sensitive to the increase of the shut-in time t_s/t_{om} . When the fluid lag vanishes at $t_s/t_{om}\approx 1$, ℓ_s/ℓ_a converges towards zero-lag solutions, and one obtains the same conclusion as shown in Fig. 2a: a smaller \mathcal{K}_m leads to a larger difference in fracture extension between upon shut-in and at arrest.

5.3.1 Early-Time Fracture Overshoot

It is interesting to notice from Fig. 3 that the fracture length can be even larger than the theoretical arrest dimension ℓ_a at early shut-in $t/t_{om} \ll 1$ for $\mathcal{K}_m \ll 1$. Such an overshoot is associated with the strong pressure gradient inside the viscous fluid flow and a significant fluid lag. The fracture is probably not going to propagate any further after shutin with $\ell_s > \ell_a$, while the fluid front may advance towards and finally coalesce with the fracture front. If defining t_c as the critical shut-in time at which the fracture length equals the theoretical arrest length $\ell_s/\ell_a=1$, one obtains in Fig. 4 the corresponding critical shut-in time for different dimensionless toughness. t_c/t_{om} is not a monotonic function of the dimensionless toughness and reaches its maximum around $t_c/t_{om} \approx 5 \times 10^{-7}$ at $\mathcal{K}_m \approx 0.12$. Within the range of $t_s/t_{om} \in (10^{-8}, 1)$ investigated in this study, the fracture overshoot is unlikely to occur for $\mathcal{K}_m \gtrsim 0.3$. Note that such an immediate arrest was also expected in absence of a fluid lag when the fracture toughness dominates the fracture growth $(\mathcal{K}_m \gg 1 \text{ and } \ell_s/\ell_a \rightarrow 1, \text{ Fig. 2}).$

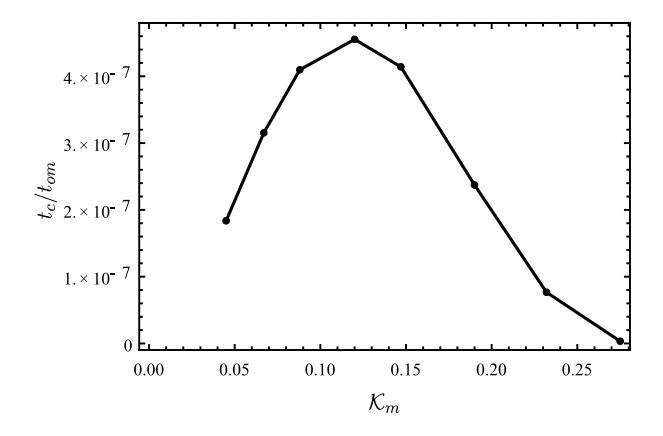


Fig. 4 Dependence of the critical shut-in time t_c on the dimensionless toughness. At $t_s = t_c$, the fracture length at shut-in equals the theoretical fracture dimension at arrest (25)

When the shut-in occurs later than the critical time $t_s > t_c$, the fracture length at shut-in again drops below the theoretical arrest extension $\ell_s < \ell_a$. The fracture probably propagates further with an increasing fluid fraction until it reaches the arrest dimension $\ell = \ell_a$.

5.3.2 Temporary Arrest and Continuous Growth Upon Shut-In

For later shut-in time or dimensionless toughness with intermediate values, the fracture overshoot is less likely to occur, yet other propagation patterns may emerge depending on the interplay between \mathcal{K}_m , t_s/t_{om} and t/t_{om} . In the following, one investigates numerically the fracture behaviour throughout the shut-in process and focuses on the effect of dimensionless shut-in time $\zeta = t_s/t_{om}$ by fixing the dimensionless toughness $\mathcal{K}_m = 0.232$.

Figure 5 shows the time evolution of the fracture length, volume efficiency, and fluid fraction corresponding to different shut-in moments. The volume efficiency decreases with time due to the increased fluid fraction inside the fracture. Moreover, the fracture presents three distinct propagation patterns after shut-in: an immediate arrest, a temporary arrest (characterized by a significant decrease in fracture front velocity upon shut-in and followed by a restart of the propagation), and direct post-shut-in propagation (with a negligible or zero delay in time after the stop of injection).

These different propagation patterns are also reflected in the evolution of width and fluid pressure profiles (Fig. 6). For the immediate fracture arrest at early shut-in time $t_s/t_{om} \ll 1$, the fracture extension upon shut-in is larger than the arrest dimension (25) due to a strong viscosity effect and a significant fluid lag. The fluid front continues approaching the fracture front after the stop of injection while the fracture tips stay at their original position. When the fluid and fracture fronts coalesce at large time, the pressure becomes uniform inside the fracture yet is not sufficiently large (resulting from the mass balance of fluid) to trigger the propagation due to a stress intensity factor smaller than the fracture toughness at the fracture tip.

At relatively larger shut-in time, the fracture extent upon shut-in is shorter than the final dimension at arrest (25). The fracture experiences a temporary arrest followed by a restart of propagation. Upon shut-in, the fluid front is far from the fracture front and the stress intensity factor is not sufficiently large to trigger the propagation. The fracture front thus stops growing while the fluid front keeps advancing towards the fracture tip (Fig. 6). When the fluid fraction is large enough such that the propagation condition is once again fulfilled, the fracture extent restarts to grow towards the final arrest dimension. Note that this step-wise feature of the hydraulic fracture growth with a significant fluid lag has not been reported before. It is different from the piece-wise nature of



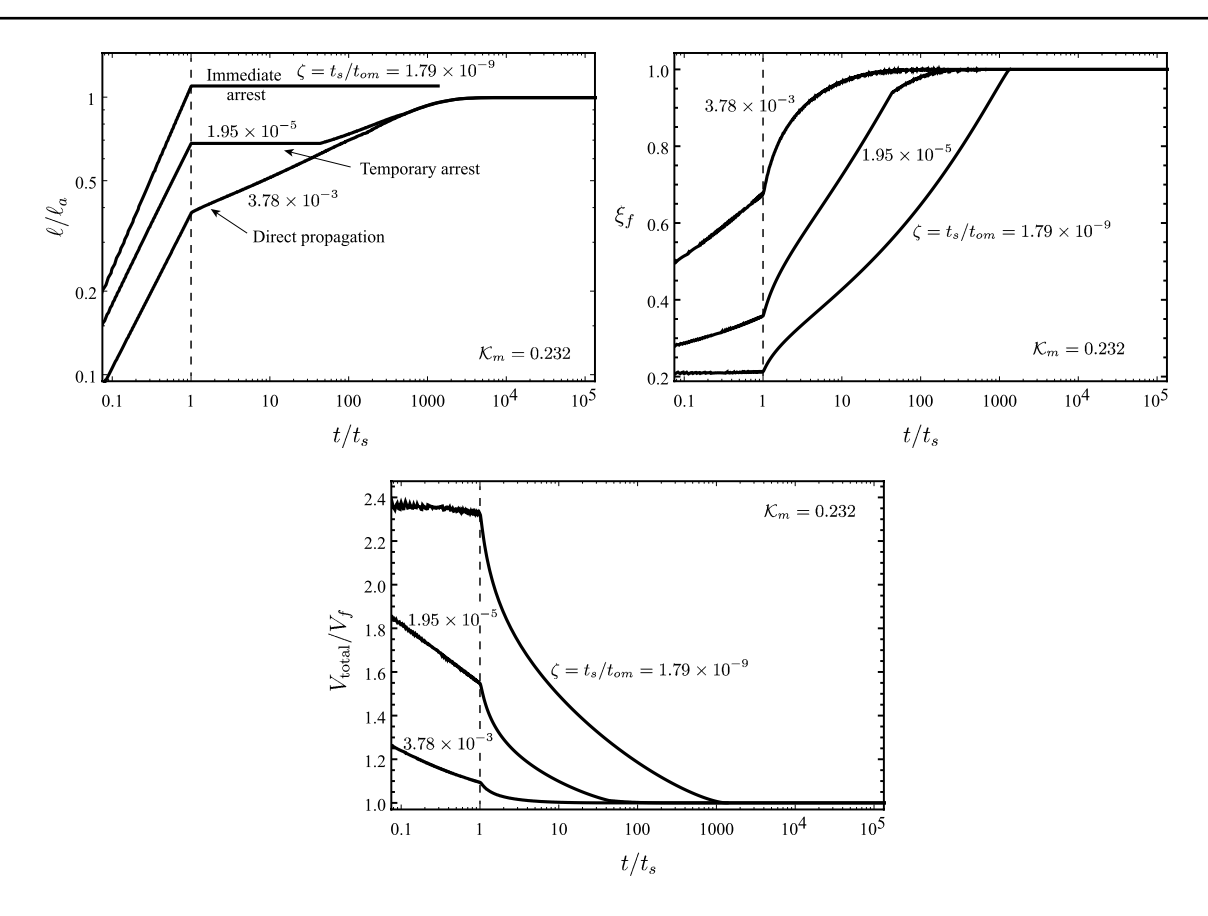


Fig. 5 Time evolution of the fracture half-length, fluid fraction and volume efficiency parameter for K_m with different shut-in time $\zeta = t_s/t_{om}$. The vertical dashed line indicates the shut-in time

the fracture dynamics (Cao et al. 2017; Peruzzo et al. 2019a, b) and the piece-wise quasi-static fracture growth related to material heterogeneity (Da Fies et al. 2022a, b, for example).

At late shut-in time, the fracture experiences a direct postshut-in propagation followed by the final fracture arrest. The fluid lag is small at the time of shut-in, which facilitates the transition of the fracture growth to zero-lag solutions (Fig. 6). Note that similar continuous propagation after the shut-in with the presence of a fluid lag has already been observed in laboratory hydraulic fracture experiments (Liu 2021; Liu and Lecampion 2023).

For all these propagation patterns shown in Fig. 6, the elastic energy stored prior to the shut-in is released through the deflation of the fracture opening. The fluid front continues to advance towards the fracture tip, which leads to an increase in the fluid fraction and a drop in the pressure gradient inside the

fluid flow. As a result, the dominated width asymptote also evolves with time.

Linear hydraulic fracture mechanics (Detournay 2016, and references therein) point out that the fracture width may present k-, m- and o-asymptote characterized respectively by fracture toughness, viscous fluid flow, and fluid lag. All these asymptotes are present during the post-shut-in growth of the fracture as shown in Fig. 7. At early time of the shut-in, the o-asymptote dominates the width profile due to a significant fluid lag. As the fluid lag vanishes, the viscous fluid flow becomes the dominant mechanism at intermediate time, and the width is then better characterized by the m-asymptote. As the fracture approaches the final arrest, the spatial pressure gradient inside the fracture decreases with time and becomes nearly zero. The fracture width can be thus approximated by a uniformly pressurized linear elastic solution, which is associated with the k-asymptote.



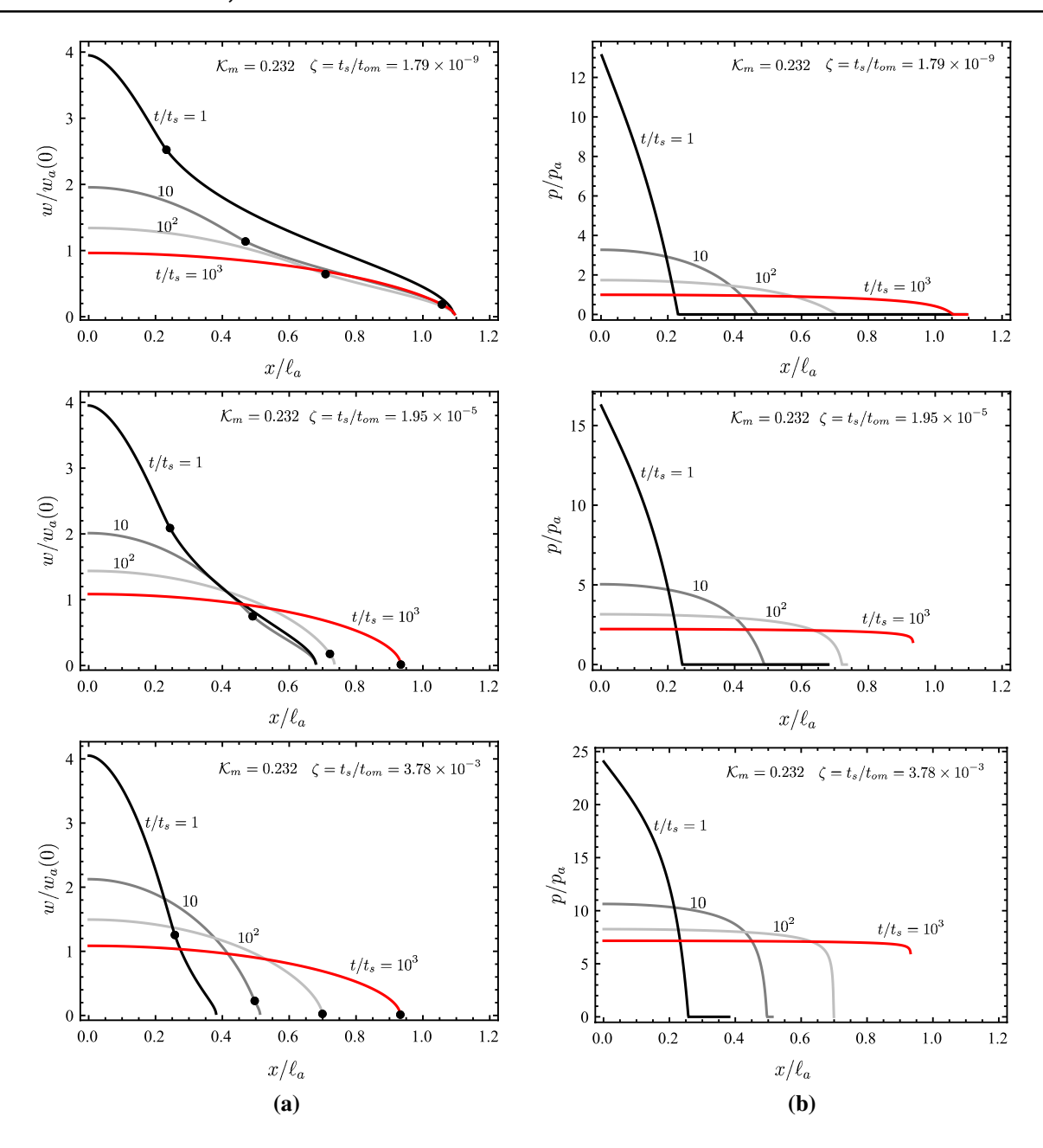


Fig. 6 Spatial profiles of **a** the dimensionless fracture opening and **b** fluid pressure for $K_m = 0.232$ at different shut-in time $\zeta = t_s/t_{om}$ corresponding to fracture behaviour such as immediate arrest, temporary arrest, and direct propagation after the shut-in. The black curve indi-

cates the spatial profile at the time of shut-in t_s , while the red curve represents the profile at $t = 1000t_s$. The black dots on the width profiles indicate their fluid front position

5.3.3 Three Post-shut-in Propagation Patterns in the Parametric Space

The fracture propagation pattern after shut-in is a function of both the shut-in time t_s/t_{om} (Fig. 5) and the dimensionless toughness \mathcal{K}_m . How the three patterns locate in the $t_s/t_{om}-\mathcal{K}_m$ parametric space will be discussed in the following.

The immediate arrest is very likely to occur at early time $t_s/t_{om} \ll 1$ for $\mathcal{K}_m \ll 1$ associated with an overshoot of the fracture extent due to a strong pressure gradient in the viscous fluid. This immediate arrest will disappear for later shut-in or larger dimensionless toughness and can be approximately constrained by the critical timescale t_c (Fig. 4). In absence of a fluid lag, the immediate arrest also occurs at large dimensionless toughness with little viscous fluid flow. Here one sets this immediate arrest limit



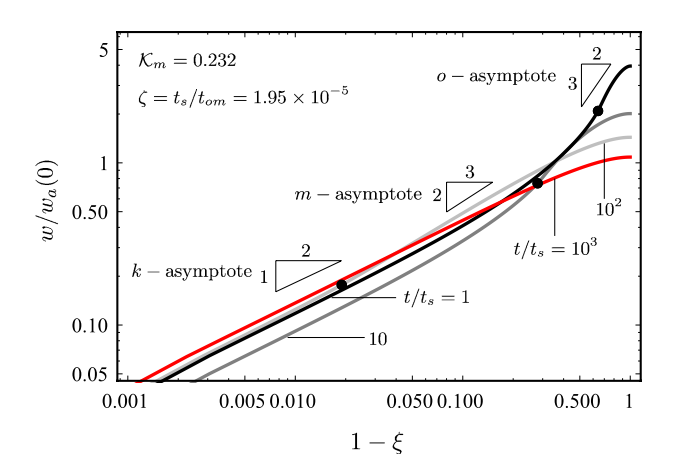
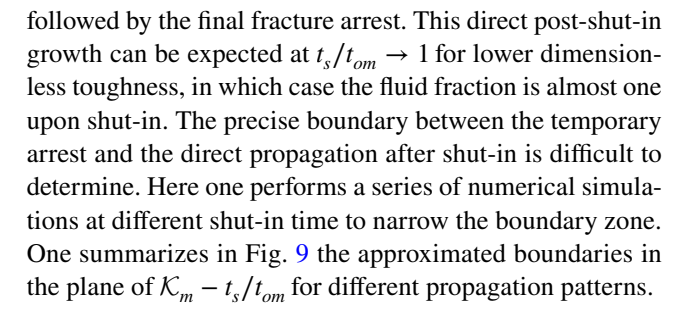


Fig. 7 Various width asymptotes corresponding to different time after the shut-in for $K_m = 0.232$ and $\zeta = t_s/t_{om} = 1.95 \times 10^{-5}$. The k-, m-, and o-asymptote represent respectively the width asymptote dominated by fracture toughness, fluid viscosity, and fluid lag. The black dots indicate the fluid front positions of different width profiles

as $K_m = 4.3$, which represents the validity of the zero-viscosity solutions for a plane-strain hydraulic fracture (Garagash 2006a).

The temporary arrest/delayed propagation most likely occurs for medium dimensionless toughness and medium range of the shut-in time t_s/t_{om} . One defines t_r as the restart time of fracture propagation and displays in Fig. 8 the time ratio t_r/t_s and the fluid fraction $\xi_f(t=t_r)$ for different dimensionless toughness. This delayed propagation restarts later for an earlier shut-in and a lower dimensionless toughness \mathcal{K}_m . Moreover, the restart of propagation does not necessarily require zero fluid lag.

When $\mathcal{K}_m \to 1$, t_r/t_s approaches to one. The fracture is more likely to experience direct post-shut-in propagation



5.3.4 Emplacement Scaling Relation

In the following, one focuses on the evolution of emplacement scaling which of course depends on the dimensionless toughness and shut-in time.

From Eq. (25), the emplacement of a fracture at arrest will follow the relation of $w_a(0) \sim \sqrt{\ell_a}$. However, such a square-root scaling relation is not guaranteed during the hydraulic fracture propagation before and after the shutin. As shown in Fig. 10a, the zero-lag solutions follow $w(0)/w_a(0) \sim \sqrt{\ell/\ell_a}$ before the shut-in and then transitions to $w(0)/w_a(0) \sim (\ell/\ell_a)^{-1}$ due to the post-shut-in fracture deflation. The deflation period is shorter for a more toughness dominated fracture propagation with a larger dimensionless toughness. During this process, the aspect ratio of the hydraulic fracture first increases, then decreases and eventually converges to (1,1) in the $\ell/\ell_a - w(0)/w_a(0)$ plane, which indicates the theoretical fracture arrest.

Non-zero lag solutions however present a larger aspect ratio at the stop of injection compared with the zero-lag solutions. As the shut-in occurs later (an increase in $\zeta = t_s/t_{om}$), the fluid lag tends to vanish and the emplacement scaling relation tends to faster converge to the zero-lag shut-in asymptote (Fig. 10b). However, when the immediate arrest

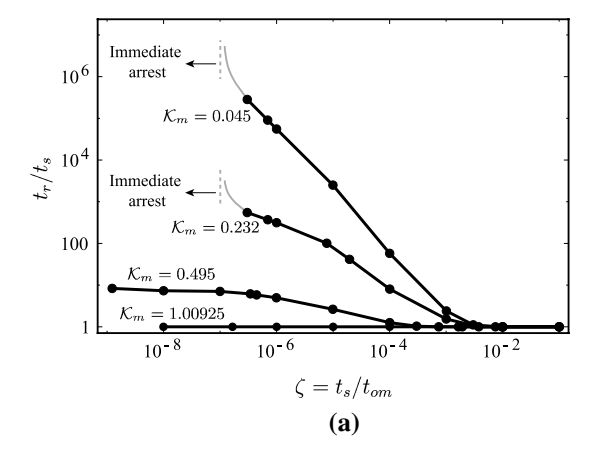
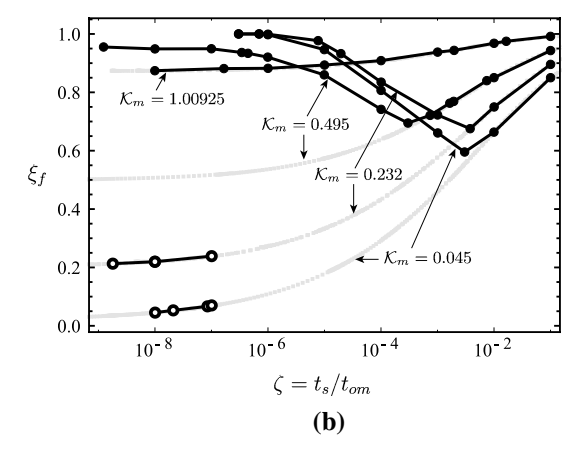


Fig. 8 a Time t_r/t_s of the restart of propagation and **b** its corresponding fluid fraction $\xi_f(t=t_r)$ as a function of the dimensionless toughness \mathcal{K}_m and shut-in time $\zeta=t_s/t_{om}$. In figure (b), the gray curves indicate the fluid fraction $\xi_f(t=t_s)$ at the time of shut-in. The solid



disks represent the fluid fraction at the restarting propagation time of the temporary arrest or at the shut-in time of the direct propagation. The empty disks represent the fluid fraction at the shut-in time characterized by the immediate fracture arrest $(t_r/t_s=\infty)$



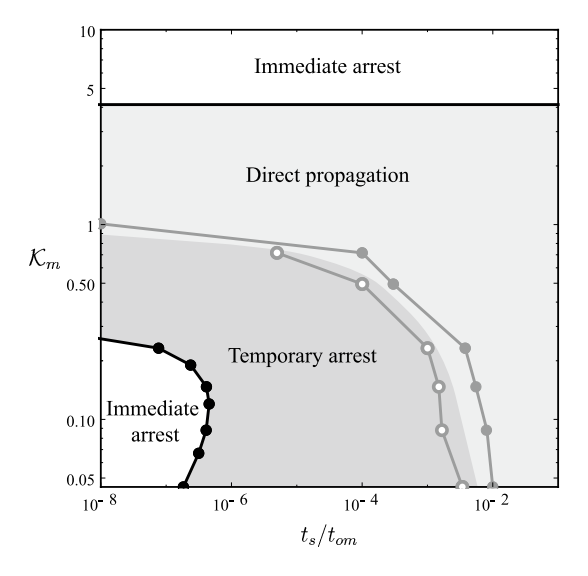


Fig. 9 Illustration of different fracture propagation patterns after shut-in as a function of the dimensionless toughness \mathcal{K}_m and shut-in time t_s/t_{om} . The gray empty and filled disks represent respectively the numerical results indicating the pattern of temporary arrest and direct propagation after shut-in. The black filled disks represent the limit of the immediate arrest associated with the fracture overshoot at early time (Fig. 4). The black horizontal line $\mathcal{K}_m = 4.3$ (Garagash 2006a) indicates the limit of toughness dominated regime which leads to the immediate arrest upon shut-in

occurs for an early shut-in with a small value of \mathcal{K}_m , the fracture extension is overshot and the fracture may present a smaller width and a longer length leading to a smaller aspect ratio at arrest with $w(0)/w_a(0) < \ell/\ell_a$.

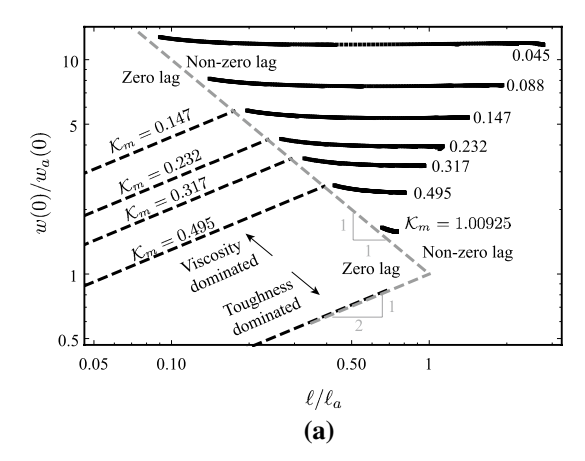


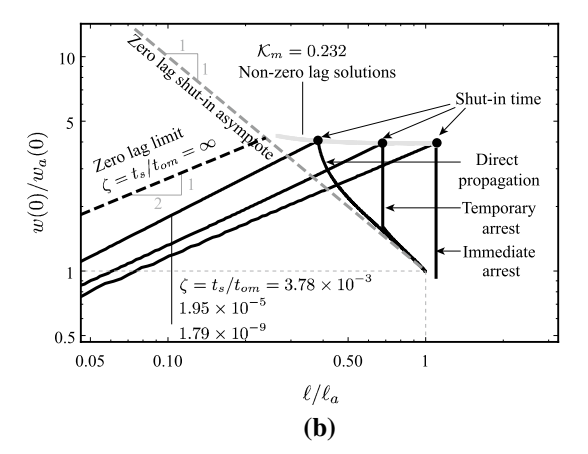
Fig. 10 a Emplacement scaling relation upon shut-in for different dimensionless toughness \mathcal{K}_m in the presence of a fluid lag (black curves). The shut-in time t_s/t_{om} increases from right to the left (for black curves). **b** Evolution of the emplacement scaling relation for $\mathcal{K}_m = 0.232$ with different shut-in time $\zeta = t_s/t_{om}$ (black solid

6 Discussion

6.1 Implications for Hydraulic Fractures at Laboratory and Field Scales

To gauge the implications for real systems, one considers typical values relevant to the laboratory- and field-scale hydraulic fractures and report in Table 2 the corresponding characteristic scales and dimensionless numbers for different types of injection.

Laboratory hydraulic fracturing injection is often performed in samples with limited dimensions under limited confinement. Assuming relatively low confinement applied on the rock samples, one considers here the injection of a highly viscous and a barely viscous fluid [with experimental conditions similar to those in Liu et al. (2020) and Liu and Lecampion (2021, 2023)] leading respectively to viscous flow/fluid lag dominated growth regime (Lab injection A) and fracture toughness dominated growth regime (Lab injection B). When the fracture toughness dominates the fracture propagation (Lab injection B), the fracture is uniformly pressurized and will immediately arrest upon shut-in. Otherwise, the fracture tends to present a temporary arrest then followed by a restart of the propagation. Note that the restart of the fracture propagation may occur quite late after the shutin. Direct observation of such temporary arrest has rarely been reported in the laboratory (Liu 2021; Liu and Lecampion 2023) since it necessitates long-period monitoring of the fracture behaviour/dimensions after the fluid shut-in. Apart from the temporary arrest, an immediate arrest of the fracture front may also likely occur in lag/viscosity dominated experiments like Lab injection A: for an early shut-in



curves). The black and gray dashed lines in $\bf a$ and $\bf b$ represent respectively the evolution of the zero lag emplacement scaling relation before (with a scaling relation of 1/2) and after shut-in (with a scaling relation of -1)



Table 2 Examples of characteristic scales for laboratory- and field-scale hydraulic fracturing injections and their possible propagation patterns after shut-in

	Fracturing fluid	μ (Pa s)	$Q_o ({ m m}^3 { m s}^{-1} { m m}$	σ_o (MPa)	Injection duration
Lab injection A	Silicone oil	1000	1.0×10^{-9}	0.1	600–1800 s
Lab injection B	Glycerol	0.6	1.0×10^{-9}	5	30–1800 s
Micro-HF test	Slick water	0.005	1.0×10^{-5}	20	60–240 s
Well stimulation	Slick water	1	1.0×10^{-3}	20	1800–7200 s
Magma dike A	Magma	300	2	20	0.5 h
Magma dike B	Magma	0.1	0.02	20	30 d
	\mathcal{K}_m	t_{om} (s)		t_s/t_{om}	Possible growth patterns after shut-in
Lab injection A	0.004	1.4×10^{11}	l	~ 10 ⁻⁸	Immediate arrest or temporary arrest
Lab injection B	4.0	250		$\sim 0.1 - 10$	Immediate arrest
Micro-HF test	1.32	0.03		$\sim 10^2 - 10^4$	Direct propagation or immediate arrest
Well stimulation	0.11	6.5		$\sim 10^2 - 10^4$	Direct propagation
Magma dike A	0.004	1.95×10	3	~0.1-1	Temporary arrest or direct propagation
Magma dike B	0.09	0.65		$\sim 10^{6}$	Direct propagation

One takes E=60 GPa, $\nu=0.3$, $K_{\rm Ic}=1.5$ MPa m^{1/2} for most cases except Lab injection A where one takes instead E=100 GPa, $\nu=0.3$ and $K_{\rm Ic}=0.6$ MPa m^{1/2}

 $t_s/t_{om} \ll 1$, the fracture front may stop growing immediately at the stop of injection, and the fluid front gradually evolves towards the fracture front until it catches up with the fracture tip or reaches the sample boundary.

Most in-situ industrial injections are performed at a depth from 1.5 km down to 4 km, corresponding to a minimum confining stress of around tens of MPa. Under such confinement, one evaluates the characteristic scales for two injection scenarios: a micro-HF test with the injection of a less-viscous type of slick water, and a well stimulation operation with the injection of a more-viscous type of slick water. As shown in Table 2, in both cases, the timescale t_{om} is small and indicates the presence of a negligible fluid lag. The temporary arrest behaviour, which necessitates the presence of a fluid lag, is possibly excluded in typical industrial injections. For the micro-HF test, the injection is often performed at a small injection rate, and the fracture growth is characterized by a dimensionless toughness \mathcal{K}_m of less than two. As a result, the fracture either continues to propagate after the shut-in or stops growing immediately when the fracture toughness dominates the propagation at the stop of injection (which happens under the conditions of a smaller injection rate, less viscous fluid, and rocks with larger fracture toughness). Different from the micro-HF test, the well stimulation is characterized by a larger injection rate and a longer injection period. The viscosity likely governs the fracture growth upon shut-in, and the fracture may directly continue propagating afterwards. In terms of the injection efficiency (30), the fluid lag vanishes fast in both scenarios, and the fracture volume most likely equals to or becomes smaller than the volume of injected fluid due to a probable

leak-off. The injection efficiency is thus probably smaller than one for most industrial injections.

When neglecting buoyancy, magma-driven geological structures, such as sills and dikes, can be approximated by a hydraulic fracture driven by a pulse fluid injection in the plane-strain state (Rubin 1993; Bunger and Cruden 2011). The formation of these geological structures is often characterized by a significant cavitation between the magma front and the fracture front due to the large viscosity of magma and little leak-off (Rubin 1993). Previous studies point out that dikes present a wide range of distribution in the emplacement scaling relations and aspect ratios (Olson 2003; Scholz 2010; Olson and Schultz 2011; Rivalta et al. 2015). This has been attributed to the scale-related fracture apparent toughness of geological formations, the interplay between the process zone and roughness-induced fluid flow deviation (from Poiseuille's law), and the mixed mode fracturing at small scales (Liu et al. 2019; Liu and Lecampion 2021, 2022; Arachchige et al. 2022). In the following, assuming constant fracture energy, one focuses on the influence of the fluid lag on the dike emplacement. As shown in Table 2, one considers two scenarios related to the magma dike formation under relatively low tectonic stresses. One scenario is characterized by a short-period injection of basaltic magma with a large flux (Magma dike A), and the other is characterized by a long-period injection of a lowend viscous magma (similar to that of Kimberlite) with a small flux (Magma dike B) (Rivalta et al. 2015). For both scenarios, the growth of magma dikes at the shut-in is very likely dominated by the viscous fluid flow and the fluid lag can not be neglected at least during the pulse injection stage.



In the case of a very short injection with an extremely large flux, the dike may probably present a temporary arrest. Otherwise, it tends to propagate continuously after the shut-in followed by a permanent arrest. Such a temporary arrest may last for quite a long time, and the magma may cool off and solidify before the restart of the propagation. It is thus very likely that the final geometry of the dikes deviates from the square-root emplacement scaling relation $w(0) \sim \sqrt{\ell}$ and presents a different aspect ratio. This partly explains the wide range of dike emplacement/aspect ratio observed in nature. As a result, fracture toughness estimation based on linear elastic fracture mechanics and dikes' emplacement may not be precise. Further investigation accounting for the injection/shut-in history and fluid lag is necessary to better decipher the relation between the emplacement scaling and fracture toughness.

6.2 Effects of a Possible Fluid Leak-Off

In this study, one assumes an impermeable medium and zero fluid leak. When accounting for a permeable medium, the fracture growth may present more complex behaviours due to fluid leak-off. Adachi and Detournay (2008), Hu and Garagash (2010) and Chen et al. (2018) account for the fluid leaking into the surrounding medium in the case of zero fluid shut-in for a plane-strain hydraulic fracture. They approximate the fluid leak-off using Carter's law (Howard and Fast 1957; Lecampion et al. 2018), which is a 1-D approximation of the fluid diffusion into the medium. The local fluid continuity equation thus writes as follows.

$$\frac{\partial w}{\partial t} + \frac{\partial q}{\partial x} + \frac{C'}{\sqrt{t - t_0(x)}} = 0, \, x \in [0, \ell_f], \, t > t_0(x) \tag{31}$$

where t_0 is the arrival time of the fluid front at the position x and $C' = 2C_L$ is the effective leak-off coefficient with C_L the fluid loss constant which can be calibrated from hydraulic fracture injection tests. Such fluid leak-off is a time-dependent process and introduces another timescale $t_{\bar{n}m}$ in the dimensional analysis (Adachi and Detournay 2008; Hu and Garagash 2010; Chen et al. 2018; Peirce and Detournay 2022a):

$$t_{m\tilde{m}} = \frac{\mu' Q_o^3}{E' C'^6} \tag{32}$$

This timescale characterizes the transition between storage growth regimes (OMK) and leak-off regimes $(\tilde{O}\tilde{M}\tilde{K})$, where $\tilde{O}\tilde{M}\tilde{K}$ correspond to the leak-off regimes characterized respectively by a significant fluid lag and the dominant effects of viscous fluid flow and fracture surface creation. In the absence of fluid shut-in, the fracture growth transitions between the six distinct growth regimes $(OMK-\tilde{O}\tilde{M}\tilde{K})$ depending on the interplay among K_m , t_{om} and $t_{m\bar{m}}$. Detailed

information on these fracture growth transitions can be found in Adachi and Detournay (2008), Hu and Garagash (2010) and Chen et al. (2018).

In the presence of fluid shut-in, the fluid leak-off tends to favour an immediate fracture arrest upon shut-in, and may even result in the disappearance of the temporary arrest and the continuous propagation after the stop of fluid injection. In addition, as the stress intensity factor at the fracture tip drops from the fracture toughness K_{Lc} to zero, fracture deflation and recession may occur, as previously discussed in Peirce and Detournay (2022a) assuming zero fluid lag. The post-shut-in fracture behaviour thus results from the interplay among the dimensionless toughness \mathcal{K}_m , the shut-in time t_s , the timescale characterizing the coalescence of the fracture and fluid fronts t_{om} , and the leak-off timescale $t_{m\tilde{m}}$. Only when the leak-off timescale is significantly greater than the other timescales $(t_{m\tilde{m}} \gg t_s)$ $t_{m\tilde{m}} \gg t_{om}$) can the fracture growth be approximated by the zero leak-off solutions reported in this study.

7 Conclusions

One has investigated the growth of a plane-strain hydraulic fracture after shut-in by accounting for the possible presence of a fluid lag. One assumes that the fracture propagates in an impermeable medium and is driven under a constant injection rate before shut-in. After shut-in, the fracture presents a deflation of fracture opening and a continuous advancement of fluid front towards the fracture tip. Three propagation patterns emerge with respect to the fracture front: an immediate arrest, a temporary arrest followed by a restart of fracture propagation, and a continuous post-shut-in fracture growth. The fracture behaviour depends on three dimensionless parameters: the dimensionless toughness \mathcal{K}_m which characterizes the energy dissipation between the creation of fracture surfaces and the viscous fluid flow prior to the shut-in, the shut-in time t_s/t_{om} which characterizes the relative position of the fluid front upon shut-in (for a given K_m), and the dimensionless time t/t_s . The immediate fracture arrest occurs when toughness dominates the fracture growth ($\mathcal{K}_m > 4.3$) and when the fracture front is overshot at early time due to a significant fluid lag and a strong viscous effect ($K_m < 0.3$ with $t_s/t_{om} \lesssim 10^{-7}$ for $t_s/t_{om} \in [10^{-8}, 1]$). For later shutin time and larger dimensionless toughness, the fracture may also experience a post-shut-in temporary arrest or a direct propagation before the final arrest. A smaller dimensionless toughness \mathcal{K}_m or an earlier shut-in t_s/t_{om} tends to favour the presence of a temporary arrest and extend the arrest period. Different propagation patterns result in various fracture dimensions and aspect ratios, which may possibly explain the wide range of emplacement scaling



relations and derived apparent toughness for magmadriven dikes. The results reported in this study may also help guide the design and interpretation of laboratory hydraulic fracturing experiments in the presence of a nonnegligible fluid lag (Liu 2021; Liu and Lecampion 2023).

Appendix 1: Zero-Lag Shut-In Solutions in the State of Plane-Strain

Gauss—Chebyshev quadrature combined with Barycentric interpolation techniques provides an efficient way to solve elastic boundary integral solutions arising in fracture problems (Viesca and Garagash 2018; Liu and Brantut 2023). It has been recently applied to semi-infinite (Garagash 2019) and finite hydraulic fracture propagation problems (Liu et al. 2019; Kanin et al. 2021; Möri and Lecampion 2021; Pereira and Lecampion 2021; Liu and Lu 2023), illustrating spectral accuracy and efficiency in large timespan semi-analytical investigations. In this work, following Liu et al. (2019) and Liu and Lu (2023) one uses the first type Gauss—Chebyshev quadrature T_k to discretize the fracture. It consists of two sets of nodes whose values are in the range of (-1, 1).

$$s_{j} = \cos\left(\frac{\pi(j-1/2)}{n}\right), \quad j = 1, \dots, n;$$

$$z_{i} = \cos\left(\frac{\pi i}{n}\right), \quad i = 1, \dots, n-1,$$
(33)

where n is the number of unknowns. These nodes naturally include the dislocation singularity appearing at the fracture tips in linear elastic fracture mechanics.

$$\frac{\mathrm{d}w}{\mathrm{d}s} = \omega(s)F(s), \quad \omega(s) = \frac{1}{\sqrt{1 - s^2}}$$
(34)

where F(s) is an non-singular unknown. Following Viesca and Garagash (2018) and Liu et al. (2019), one discretizes the governing equations as follows.

Elasticity

$$\frac{4\ell}{E'}\mathbf{p} = \mathbb{H} \cdot \mathbf{F}, \quad \mathbb{H} = \left\{ \frac{1}{n} \frac{1}{z_i - s_i} \right\}$$
 (35)

• Lubrication flow

$$-\mathbf{z}\frac{\partial}{\partial t}(\mathbb{S}\cdot\mathbf{F}) + \frac{\partial}{\partial t}(\mathbb{S}\cdot(\mathbf{s}\,\mathbf{F})) + \frac{\dot{\ell}}{\ell}(\mathbb{S}\cdot(\mathbf{s}\,\mathbf{F}))$$

$$= -\frac{E'}{4u'\ell^3}(\mathbb{S}\cdot\mathbf{F})^3(\mathbb{D}\cdot\mathbb{H}\cdot\mathbf{F})$$
(36)

• Global continuity equation and shut-in condition



$$\mathbf{S}_A \cdot (\mathbf{s} \, \mathbf{F}) + \frac{V_f}{\ell} = 0 \tag{37}$$

where $V_f = Q_o t$ before the shut-in time t_s . Such a constant flux before shut-in and the zero flux condition after shut-in is applied via a smoothed step function f.

$$V_f = Q_o t (1 - f(t/t_s - 1)) + Q_o t_s f(t/t_s - 1),$$

$$f(m) = 1/(1 + \exp(-2hm))$$
(38)

h = 130 is a dimensionless parameter one sets to model the sudden shut-in of the fluid injection at $t = t_s$.

• Propagation criterion

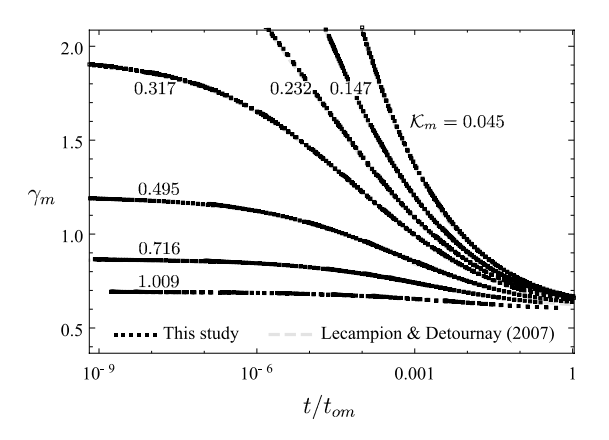
$$\mathbf{Q} \cdot \mathbf{F} = -\frac{1}{\sqrt{2}} \frac{K' \ell^{1/2}}{E'} \tag{39}$$

 \mathbb{H} is the Hilbert transform matrix. \mathbb{S} and \mathbb{S}_A are integration operators, \mathbb{D} is the differentiation operator, and \mathbb{Q} is the extrapolation operator, see the expressions with the same notations in Liu et al. (2019) for more details.

The unknowns of these ordinary differential equations therefore become the unknown vector $\mathbf{F} = \{F(s_j)\}, j = 1, ..., n$ and the fracture dimension ℓ . One uses n = 80 for all the zero-lag simulations presented in this work.

Appendix 2: Model Validation in the Case of Zero Fluid Shut-In

Previous numerical work (Lecampion and Detournay 2007; Gordeliy and Detournay 2011) sets the early-time similarity solutions (Garagash 2006b) as the initial condition when simulating the growth of a hydraulic fracture in the presence of a fluid lag. Shen (2014) and Mollaali and Shen (2018) argue that the hydraulic fracture growth is insensitive to the pressure profile of the initial condition and use the elastic solution corresponding to a pressure profile with a constant gradient and a fluid lag. In this study, one adopts the static elastic solution of a uniformly pressurized fracture as the initial condition. It is a natural choice when there is not much prior knowledge available about the exact fracture growth, and it corresponds to the state of a small notch full of fluid prior to injection, which is often the case in laboratory hydraulic fracturing experiments (Liu and Lecampion 2022). This initial condition introduces a small amount of fluid in addition to the injected fluid. As the fracture grows, the fluid mass introduced by the initial condition becomes negligible compared to the total injected fluid mass. Moreover, the numerical solver simulates the spontaneous nucleation of the fluid lag and makes the pressure profile inside the fracture quickly converge toward the exact solution of the problem with a non-zero pressure gradient and a fluid lag.



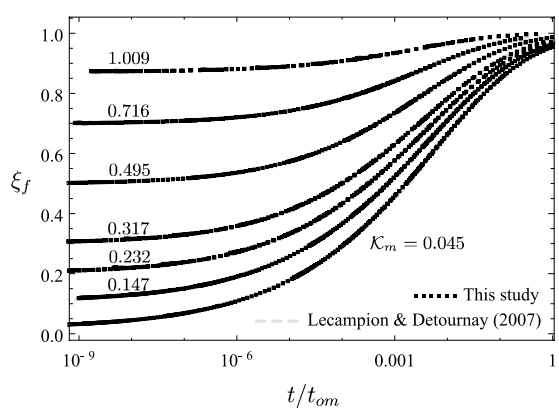


Fig. 11 Time evolution of \mathbf{a} the half fracture length in the viscosity scaling and \mathbf{b} fluid fraction for different dimensionless toughness \mathcal{K}_m for the case of zero fluid shut-in

However, the numerical results may deviate from the exact solutions in the first few time steps due to the initial condition and the relatively low mesh resolution inside the fracture. To minimize this deviation, one assumes a very small flaw size with the fluid pressure p_f only slightly larger than the minimum confining stress σ_o at the initial state, which minimizes the fluid mass perturbation. One also removes the numerical results of the first several time steps, which are significantly influenced by the initial condition. Moreover, to simulate the fluid shut-in, fluid injection is halted only when the fluid mass introduced by the initial condition becomes negligible relative to the total injected fluid mass. These measures ensure that the initial condition has a negligible impact on the fracture behaviours.

One benchmarks the numerical scheme for the case of zero fluid shut-in and compares the results obtained in this study with those reported by Lecampion and Detournay (2007), who employ the early-time similarity solutions as the initial condition. As shown in Fig. 11, the numerical results agree very well with each other, indicating that the initial condition has a negligible influence on the reported fracture growth. It is worth noting that Fig. 3 is obtained by processing the same numerical results displayed in Fig. 11. This ensures that the early-time fracture overshoot ($\ell_s > \ell_a$) and the potential of post-shut-in fracture extension ($\ell_s < \ell_a$) as shown in Fig. 3 are not influenced by the initial condition, and these behaviours reflect the different growth patterns of hydraulic fractures after fluid shut-in.

Acknowledgements The author would like to appreciate the facility support provided by the Department of Earth Sciences at University College of London. The author also thanks Brice Lecampion for the discussion at the early stage of this research.

Declarations

Conflict of interest The author has no competing interests to declare that are relevant to the content of this article.

Open Access This article is licensed under a Creative Commons Attribution 4.0 International License, which permits use, sharing, adaptation, distribution and reproduction in any medium or format, as long as you give appropriate credit to the original author(s) and the source, provide a link to the Creative Commons licence, and indicate if changes were made. The images or other third party material in this article are included in the article's Creative Commons licence, unless indicated otherwise in a credit line to the material. If material is not included in the article's Creative Commons licence and your intended use is not permitted by statutory regulation or exceeds the permitted use, you will need to obtain permission directly from the copyright holder. To view a copy of this licence, visit http://creativecommons.org/licenses/by/4.0/.

References

Adachi JI, Detournay E (2008) Plane strain propagation of a hydraulic fracture in a permeable rock. Eng Fract Mech 75(16):4666–4694
Arachchige UN, Cruden AR, Weinberg R, Slim A, Köpping J (2022)
Saucers, fingers and lobes: new insights on sill emplacement from scaled laboratory experiments. J Geophys Res Solid Earth 2022:e2022JB024421

Bunger AP, Cruden AR (2011) Modeling the growth of laccoliths and large mafic sills: role of magma body forces. J Geophys Res Solid Earth 116(B2):1

Bunger AP, Detournay E (2007) Early-time solution for a radial hydraulic fracture. J Eng Mech 133(5):534–540

Bunger AP, Gordeliy E, Detournay E (2013) Comparison between laboratory experiments and coupled simulations of saucer-shaped hydraulic fractures in homogeneous brittle-elastic solids. J Mech Phys Solids 61(7):1636–1654

Cao TD, Milanese E, Remij EW, Rizzato P, Remmers JJ, Simoni L, Huyghe JM, Hussain F, Schrefler BA (2017) Interaction between crack tip advancement and fluid flow in fracturing saturated porous media. Mech Res Commun 80:24–37



- Chen B, Barron AR, Owen D, Li C (2018) Propagation of a plane strain hydraulic fracture with a fluid lag in permeable rock. J Appl Mech 85(9):091003
- Da Fies G, Dutko M, Peck D (2022a) Averaging-based approach to toughness homogenisation for radial hydraulic fracture. Preprint arXiv:2211.03114
- Da Fies G, Peck D, Dutko M, Mishuris G (2022b) A temporal averaging—based approach to toughness homogenisation in heterogeneous material. Math Mech Solids 2022:10812865221117552
- Detournay E (2004) Propagation regimes of fluid-driven fractures in impermeable rocks. Int J Geomech 4(1):35–45
- Detournay E (2016) Mechanics of hydraulic fractures. Annu Rev Fluid Mech 48:311–339
- Garagash DI (2006a) Plane-strain propagation of a fluid-driven fracture during injection and shut-in: asymptotics of large toughness. Eng Fract Mech 73(4):456–481
- Garagash DI (2006b) Propagation of a plane-strain hydraulic fracture with a fluid lag: early-time solution. Int J Solids Struct 43(18–19):5811–5835
- Garagash DI (2019) Cohesive-zone effects in hydraulic fracture propagation. J Mech Phys Solids 133(103):727
- Garagash DI, Detournay E (2005) Plane-strain propagation of a fluid-driven fracture: small toughness solution. J Appl Mech 72(6):916–928
- Gordeliy E, Detournay E (2011) A fixed grid algorithm for simulating the propagation of a shallow hydraulic fracture with a fluid lag. Int J Numer Anal Meth Geomech 35(5):602–629
- Gordeliy E, Abbas S, Peirce A (2019) Modeling nonplanar hydraulic fracture propagation using the XFEM: an implicit level-set algorithm and fracture tip asymptotics. Int J Solids Struct 159:135–155
- Hills D, Kelly P, Dai D, Korsunsky A (1996) Solution of crack problems: the distributed dislocation technique. J Appl Mech 1:1
- Howard GC, Fast CR (1957) Optimum fluid characteristics for fracture extension. In: Drilling and production practice, OnePetro
- Hu J, Garagash DI (2010) Plane-strain propagation of a fluid-driven crack in a permeable rock with fracture toughness. J Eng Mech 136(9):1152–1166
- Kanin EA, Dontsov EV, Garagash DI, Osiptsov AA (2021) A radial hydraulic fracture driven by a Herschel–Bulkley fluid. J Nonnewton Fluid Mech 295(104):620
- Lecampion B, Detournay E (2007) An implicit algorithm for the propagation of a hydraulic fracture with a fluid lag. Comput Methods Appl Mech Eng 196(49–52):4863–4880
- Lecampion B, Bunger A, Zhang X (2018) Numerical methods for hydraulic fracture propagation: a review of recent trends. J Nat Gas Sci Eng 49:66–83
- Liu D (2021) Hydraulic fracture growth in quasi-brittle materials. PhD thesis, EPFL, Lausanne, Switzerland. https://doi.org/10.5075/epfl-thesis-8360
- Liu D, Brantut N (2023) Micromechanical controls on the brittle-plastic transition in rocks. Geophys J Int 234(1):562–584
- Liu D, Lecampion B (2019a) Growth of a radial hydraulic fracture accounting for the viscous fluid flow in a rough cohesive zone. In: ARMA-CUPB geothermal international conference, ARMA, ARMA-CUPB-19-4210
- Liu D, Lecampion B (2019b) Propagation of a plane-strain hydraulic fracture accounting for the presence of a cohesive zone and a fluid lag. In: 53rd US rock mechanics/geomechanics symposium, ARMA, ARMA-2019-0103

- Liu D, Lecampion B (2021) Propagation of a plane-strain hydraulic fracture accounting for a rough cohesive zone. J Mech Phys Solids 149(104):322
- Liu D, Lecampion B (2022) Laboratory investigation of hydraulic fracture growth in Zimbabwe gabbro. J Geophys Res Solid Earth 1:e2022JB025678
- Liu D, Lecampion B (2023) Measurements of the evolution of the fluid lag in laboratory hydraulic fracture experiments in rocks. Mech Hydraul Fract Exp Model Monit 1:11–23
- Liu D, Lu G (2023) Effects of velocity-dependent toughness on the preand post-shut-in growth of a hydraulic fracture. Comput Geotech 155(105):195
- Liu D, Lecampion B, Garagash DI (2019) Propagation of a fluid-driven fracture with fracture length dependent apparent toughness. Eng Fract Mech 220(106):616
- Liu D, Lecampion B, Blum T (2020) Time-lapse reconstruction of the fracture front from diffracted waves arrivals in laboratory hydraulic fracture experiments. Geophys J Int 223(1):180–196
- Mollaali M, Shen Y (2018) An Elrod–Adams-model-based method to account for the fluid lag in hydraulic fracturing in 2D and 3D. Int J Fract 211(1–2):183–202
- Möri A, Lecampion B (2021) Arrest of a radial hydraulic fracture upon shut-in of the injection. Int J Solids Struct 219:151–165
- Olson JE (2003) Sublinear scaling of fracture aperture versus length: An exception or the rule? J Geophys Res Solid Earth 108(B9):1
- Olson JE, Schultz RA (2011) Comment on "A note on the scaling relations for opening mode fractures in rock" by CH Scholz. J Struct Geol 33(10):1523–1524
- Peirce A (2022) The arrest and recession dynamics of a deflating radial hydraulic fracture in a permeable elastic medium. J Mech Phys Solids 1:104926
- Peirce A, Detournay E (2022a) The arrest and recession dynamics of a deflating hydraulic fracture in a permeable elastic medium in a state of plane strain. Int J Solids Struct 1:111906
- Peirce A, Detournay E (2022b) Sunset similarity solution for a receding hydraulic fracture. J Fluid Mech 944:1
- Pereira L, Lecampion B (2021) A plane-strain hydraulic fracture driven by a shear-thinning Carreau fluid. Int J Numer Anal Meth Geomech 45(11):1603–1623
- Peruzzo C, Cao DT, Milanese E, Favia P, Pesavento F, Hussain F, Schrefler BA (2019a) Dynamics of fracturing saturated porous media and self-organization of rupture. Eur J Mech A/Solids 74:471–484
- Peruzzo C, Simoni L, Schrefler BA (2019b) On stepwise advancement of fractures and pressure oscillations in saturated porous media. Eng Fract Mech 215:246–250
- Rice JR (1968) Mathematical analysis in the mechanics of fracture. Fract Adv Treat 2:191–311
- Rivalta E, Dahm T (2006) Acceleration of buoyancy-driven fractures and magmatic dikes beneath the free surface. Geophys J Int 166(3):1424–1439
- Rivalta E, Taisne B, Bunger AP, Katz RF (2015) A review of mechanical models of dike propagation: schools of thought, results and future directions. Tectonophysics 638:1–42
- Rubin AM (1993) Tensile fracture of rock at high confining pressure: implications for dike propagation. J Geophys Res Solid Earth 98(B9):15919–15935
- Rubin AM (1995) Propagation of magma-filled cracks. Annu Rev Earth Planet Sci 23:287–336
- Scholz CH (2010) A note on the scaling relations for opening mode fractures in rock. J Struct Geol 32(10):1485–1487



- Shen Y (2014) A variational inequality formulation to incorporate the fluid lag in fluid-driven fracture propagation. Comput Methods Appl Mech Eng 272:17–33
- Spence D, Sharp P (1985) Self-similar solutions for elastohydrodynamic cavity flow. Proc R Soc Lond Math Phys Sci 400(1819):289-313
- Szeri AZ (2010) Fluid film lubrication. Cambridge University Press, Cambridge
- Viesca RC, Garagash DI (2018) Numerical methods for coupled fracture problems. J Mech Phys Solids 113:13–34
- Wang Z, Detournay E (2018) The tip region of a near-surface hydraulic fracture. J Appl Mech 85(4):041010

- Wang Z, Detournay E (2021) Force on a moving liquid blister. J Fluid Mech 918:1
- Zhang X, Detournay E, Jeffrey R (2002) Propagation of a penny-shaped hydraulic fracture parallel to the free-surface of an elastic half-space. Int J Fract 115(2):125–158
- Zhang X, Jeffrey R, Detournay E (2005) Propagation of a hydraulic fracture parallel to a free surface. Int J Numer Anal Methods Geomech 29(13):1317–1340

Publisher's Note Springer Nature remains neutral with regard to jurisdictional claims in published maps and institutional affiliations.

